

Hybrid Metrology for Nanostructured Optical Metasurfaces

Original

Hybrid Metrology for Nanostructured Optical Metasurfaces / Murataj, Irdi; Angelini, Angelo; Cara, Eleonora; Porro, Samuele; Beckhoff, Burkhard; Kayser, Yves; Hönicke, Philipp; Ciesielski, Richard; Gollwitzer, Christian; Soltwisch, Victor; Perez-Murano, Francesc; Fernandez-Regulez, Marta; Carignano, Stefano; Boarino, Luca; Castellino, Micaela; FERRARESE LUPI, Federico. - In: ACS APPLIED MATERIALS & INTERFACES. - ISSN 1944-8244. - STAMPA. - 15:50(2023), pp. 57992-58002. [10.1021/acsami.3c13923]

Availability:

This version is available at: 11583/2984024 since: 2023-11-23T08:23:33Z

Publisher:

ACS

Published

DOI:10.1021/acsami.3c13923

Terms of use:

This article is made available under terms and conditions as specified in the corresponding bibliographic description in the repository

Publisher copyright

(Article begins on next page)

Hybrid Metrology for Nanostructured Optical Metasurfaces

Irdi Murataj,* Angelo Angelini, Eleonora Cara, Samuele Porro, Burkhard Beckhoff, Yves Kayser, Philipp Hönicke, Richard Ciesielski, Christian Gollwitzer, Victor Soltwisch, Francesc Perez-Murano, Marta Fernandez-Regulez, Stefano Carignano, Luca Boarino, Micaela Castellino, and Federico Ferrarese Lupi*



Cite This: *ACS Appl. Mater. Interfaces* 2023, 15, 57992–58002



Read Online

ACCESS |



Metrics & More



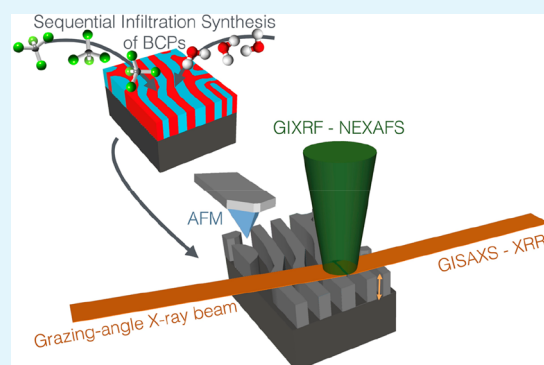
Article Recommendations



Supporting Information

ABSTRACT: Metasurfaces have garnered increasing research interest in recent years due to their remarkable advantages, such as efficient miniaturization and novel functionalities compared to traditional elements such as lenses and filters. These advantages have facilitated their rapid commercial deployment. Recent advancements in nanofabrication have enabled the reduction of optical metasurface dimensions to the nanometer scale, expanding their capabilities to cover visible wavelengths. However, the pursuit of large-scale manufacturing of metasurfaces with customizable functions presents challenges in controlling the dimensions and composition of the constituent dielectric materials. To address these challenges, the combination of block copolymer (BCP) self-assembly and sequential infiltration synthesis (SIS), offers an alternative for fabrication of high-resolution dielectric nanostructures with tailored composition and optical functionalities. However, the absence of metrological techniques capable of providing precise and reliable characterization of the refractive index of dielectric nanostructures persists. This study introduces a hybrid metrology strategy that integrates complementary synchrotron-based traceable X-ray techniques to achieve comprehensive material characterization for the determination of the refractive index on the nanoscale. To establish correlations between material functionality and their underlying chemical, compositional and dimensional properties, TiO₂ nanostructures model systems were fabricated by SIS of BCPs. The results from synchrotron-based analyses were integrated into physical models, serving as a validation scheme for laboratory-scale measurements to determine effective refractive indices of the nanoscale dielectric materials.

KEYWORDS: Block Copolymers, Sequential Infiltration Synthesis, Grazing Incidence X-ray Fluorescence, Grazing Incidence Small Angle X-ray Scattering, Synchrotron Radiation



INTRODUCTION

In the contemporary scientific research landscape of photonics, few subjects generate as significant interest as optical metamaterials, that are artificial materials characterized by subwavelength structuring that governs their optical properties.¹ The reason for this growing interest can be attributed to the limitless scientific possibilities that metasurfaces offer² and their direct impact on the economy.³ Numerous companies currently sell meta-products that address critical issues in healthcare,^{4,5} aerospace,⁶ microelectronics,^{7–9} automotive,¹⁰ and sustainable energy harvesting.¹¹ The common thread uniting these diverse applications is the need for low-cost, efficient functional materials with ultrathin features. One of the most paradigmatic cases is the development of ultrathin optical components through the use of flat metasurfaces working at visible frequencies.^{12,13} This process has been enabled by the introduction of technological advancements in nanofabrication techniques, which have allowed for the reduction of the dimensions of optical metasurfaces, expanding their capability

to cover the visible spectrum. For this purpose, numerous types of metasurfaces have been proposed, including all-dielectric^{14,15} and hyperbolic metasurfaces (HMSs)^{16,17} (Figure 1a), showing unconventional behaviors such as the photonic spin-Hall effect,¹⁸ negative refraction,^{19,20} or enhanced Purcell factor.^{21,22} The optical properties of metasurfaces are profoundly influenced by the refractive index of their dielectric elements, the so-called *meta-atoms*. This parameter assumes a pivotal role in governing the interaction of light with subwavelength structures within metasurfaces, influencing characteristics such as phase, dispersion, and polarization conversion.² Precise engineering

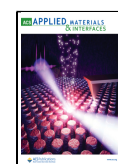
Special Issue: Block Copolymers: Building Block for Next Generation Nanotechnology

Received: September 18, 2023

Revised: October 23, 2023

Accepted: November 7, 2023

Published: November 22, 2023



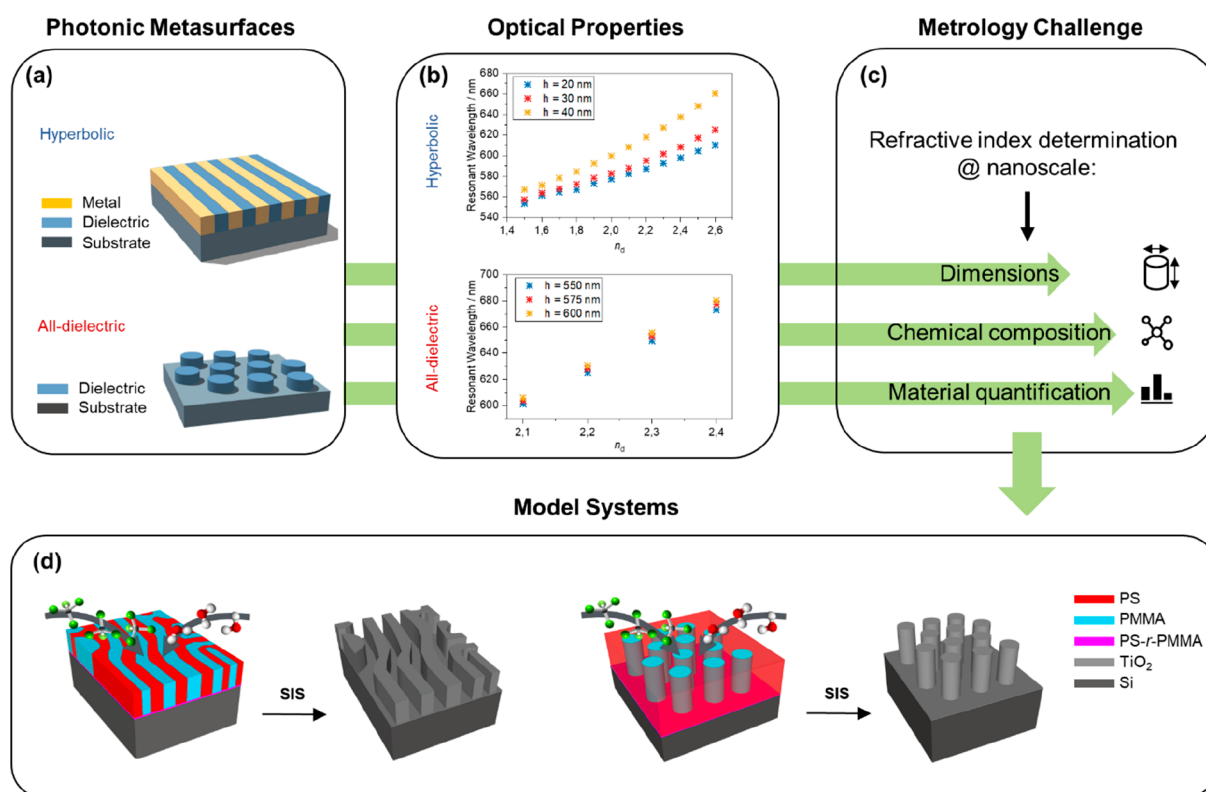


Figure 1. (a) Schematic representation of hyperbolic and all-dielectric metasurfaces. (b) Resonant wavelength variation calculated for a hyperbolic metasurface composed by alternated metal and dielectric lamellae as a function of the refractive index of the dielectric phase n_d for $h = 20$ nm (blue), $h = 30$ nm (red), and $h = 40$ nm (yellow) and resonant wavelength variation for an all-dielectric metasurfaces composed of dielectric nanocylinders as a function of the refractive index of the dielectric n_d for $h = 550$ nm (blue), $h = 575$ nm (red) and $h = 600$ nm (yellow). (c) Metrology challenge for the definition of the refractive index of nanomaterials. (d) Schematic representation of the block copolymer template in lamellar and cylindrical morphologies during the sequential infiltration synthesis (SIS) of TiO_2 in the PMMA (light-blue) nanodomains and after the uninfiltred PS (red) phase has been removed. The thin neutralization RCP layer, depicted in pink before polymer removal, is also subject to the infiltration process since it contains PMMA. The dimensions of the nanostructures, of the RCP infiltrated layer and of the substrate are exaggerated and not in scale.

of the *meta-atoms'* refractive index allows for the customization of optical responses, thereby enabling diverse functionalities including beam manipulation, polarization control, focusing, and spectral modulation. An illustrative example is presented in Figures 1b, S1, and S2, emphasizing the significant impact of the *meta-atoms'* refractive index on the resonance wavelength supported by both hyperbolic and all-dielectric metasurfaces.

Nonetheless, attaining such an advanced level of control over the refractive index requires surmounting numerous technological and metrological hurdles associated with fabricating and measuring dimensional aspects (e.g., size, height, and periodicity)^{23–26} as well as structural features (e.g., chemical state and material density)²⁷ of the *meta-atoms* (Figure 1c).

A viable strategy to overcome these technological challenges involves the precise engineering of the refractive index within the polymer nanocomposites. Specifically, employing the sequential infiltration synthesis (SIS) method, dielectric materials such as Al_2O_3 , ZnO , or TiO_2 are incorporated into self-assembled block polymers (BCPs).^{28–30} This approach enables meticulous control over both the refractive index and the dimensions of the nanostructures, including size and thickness, within nanoporous surface coatings.³¹ The SIS process employs a conventional atomic layer deposition (ALD) apparatus and involves the cyclic exposure of self-assembled BCPs to metal–organic precursors and oxidizing

agents like water. The affinity of a metal–organic precursor to the functional moiety of the polar BCP domain leads to the selective nucleation and growth of metal oxides that replicate the BCP template morphology with precision.³² In the recent past, BCPs have demonstrated their efficacy as templates for the fabrication of HMS with alternating Au/air lamellar nanostructures, which exhibit hyperbolic behavior across a wide wavelength range within the visible spectrum.³³

However, the direct determination of the effective refractive index of the resulting inorganic/inorganic nanostructures is still challenging and requires a multianalytical approach. These techniques must be capable of accurately measuring the geometric dimensions and chemical composition of the synthesized materials to obtain a comprehensive understanding of the effective refractive indexes of the nanostructures.

In this context, insights into the correlation of the chemical composition and dimensional properties of the synthesized nanostructures with their optical behavior can be provided by a hybrid metrology measurement strategy. The concept of hybrid metrology entails the utilization of two or more distinct characterization techniques for assessing an object of interest, such as a composite nanomaterial, to enhance data acquisition, minimize measurement uncertainties, or speed up the measurement process. Typically, distinct measurement techniques are inherently associated with varying measurands, even when pursuing the quantification of identical physical or

chemical quantities, as observed within the realms of dimensional, electrical, or analytical assessments.³⁴

In this study, metal oxide nanostructures were fabricated and used as model systems (reported in Figure 1d) for the development of a hybrid metrology characterization strategy. Detailed in-depth chemical and compositional analyses of the BCP-based model systems were carried out by synchrotron-based traceable grazing-incidence X-ray fluorescence (GIXRF), X-ray reflectivity (XRR), and near-edge X-ray absorption fine structure (NEXAFS) techniques. Additional grazing-incidence small-angle X-ray scattering (GISAXS) was used to measure the dimensional properties of the nanostructures. The results obtained from the synchrotron-based analyses were further employed in a hybrid metrology fashion to enable the extraction of the effective refractive index through model-assisted spectroscopic ellipsometry (SE) of vapor-phase-infiltrated BCPs with different morphologies. The reliability of the measurements was further validated against laboratory-scale measurements such as atomic force microscopy (AFM), scanning electron microscopy (SEM), and X-ray photoelectron spectroscopy (XPS). The overall combination and correlation of synchrotron-based and lab-scale techniques, independently implemented in model-assisted spectroscopic ellipsometry, offered traceability to the measurements and mutual validation.

EXPERIMENTAL SECTION

Fabrication of TiO₂ Nanostructures. TiO₂ nanostructures were synthesized via selective infiltration of BCP films using the SIS method. Silicon substrates with 100 nm-thick thermal oxide layers were cleaned in an ultrasonic bath in acetone followed by isopropyl alcohol and functionalized by an O₂ plasma treatment at 130 W for 6 min. Subsequently, a solution of α -hydroxy ω -Br polystyrene-*stat*-poly(methyl methacrylate) (PS-*stat*-PMMA) random copolymer (RCP) (18 mg in 2 mL of toluene) was spin-coated for 60 s at 3000 rpm onto the functionalized silicon oxide wafers. To promote the perpendicular orientation of lamellar and cylindrical self-assembled BCP nanostructures, two different RCPs were used, namely, FSM7 ($M_w = 14.60 \text{ kg mol}^{-1}$), with styrene fraction (f_{PS}) of 0.59 and polydispersity index (PDI) of 1.30 for lamellar BCPs, and FSM4R1 ($M_w = 19.93 \text{ kg mol}^{-1}$), with f_{PS} of 0.59 and PDI of 1.13 for cylindrical BCPs.³⁵ The synthesis of the RCPs is described elsewhere.³⁶ The grafting process was performed in a rapid thermal processing (RTP) machine Jipelec JetFirst 200 at high temperature ($T_a = 290 \text{ }^\circ\text{C}$) for an annealing time (t_a) of 300 s, in a N₂ environment with a heating rate of $15 \text{ }^\circ\text{C s}^{-1}$. Automatic cooling to room temperature was set to 240 s. The nongrafted polymeric chains were then removed by sonication in toluene for 6 min, resulting in a final grafted RCP layer thickness of $\sim 7 \text{ nm}$, as measured by spectroscopic ellipsometry. Two solutions of lamellar-forming polystyrene-*block*-poly(methyl methacrylate) (PS-*b*-PMMA) BCPs with $M_w = 146 \text{ kg mol}^{-1}$, PDI = 1.20, $f_{PS} = 0.50$ and $M_w = 160 \text{ kg mol}^{-1}$, PDI = 1.09, $f_{PS} = 0.50$ were prepared by dissolving 18 mg of BCPs in 2 mL of toluene, each. The solutions were then spin-coated at 3000 rpm for 60 s onto the FSM7-functionalized substrates, resulting in a total BCP thickness of 35 nm, as measured by spectroscopic ellipsometry. The self-assembly was promoted by RTP at $230 \text{ }^\circ\text{C}$ for 600 s in a N₂ environment with a heating ramp of $15 \text{ }^\circ\text{C s}^{-1}$ for both BCPs and automatic cooling to room temperature for 240 s. Similarly, two solutions of cylindrical forming asymmetric PS-*b*-PMMA BCPs with $M_w = 82 \text{ kg mol}^{-1}$, PDI = 1.06, $f_{PS} = 0.70$, and $M_w = 101.5 \text{ kg mol}^{-1}$, PDI = 1.09, $f_{PS} = 0.67$ were prepared by dissolving 18 mg of BCPs in 2 mL of toluene, each. The solutions were then spin-coated at 3000 rpm for 60 s onto the FSM4R1-functionalized substrates resulting in a total BCP thickness of 35 nm, as measured by spectroscopic ellipsometry. The self-assembly was promoted by RTP at $190 \text{ }^\circ\text{C}$ for 450 s in a N₂ environment with a heating ramp of $15 \text{ }^\circ\text{C s}^{-1}$ for both BCPs and automatic cooling for 240 s. All of the BCPs

used in this study were purchased from Polymer Source Inc. and employed without further purification. The selective infiltration and growth of TiO₂ inside the BCP templates was performed by SIS process conducted inside a commercial atomic layer deposition (ALD) system (Beneq TFS 200) at the process temperature of $150 \text{ }^\circ\text{C}$ using TiCl₄ as a metal-organic precursor and water as an oxidant. All four BCP templates were simultaneously processed under identical infiltration conditions for a total of 80 cycles using a microdose infiltration synthesis (MDIS) protocol.³⁷ Each cycle's timing sequence consisted of 100 repetitions of TiCl₄ pulses, lasting 100 ms each, every 100 ms and then followed by N₂ chamber purging (250 sccm) for 30 s. An identical timing sequence was used for water, as well. Subsequently, Ar plasma (100 W for 600 s) was employed to remove the polymer matrix. Through the rest of this paper the infiltrated samples obtained by SIS of BCPs with $M_w = 146 \text{ kg mol}^{-1}$, $M_w = 160 \text{ kg mol}^{-1}$, $M_w = 82 \text{ kg mol}^{-1}$, and $M_w = 101.5 \text{ kg mol}^{-1}$ will be referred to as LAM146, LAM160, CYL82, and CYL102, respectively.

Fabrication of TiO₂ Thin Films. The deposition of TiO₂ thin films was carried out on silicon substrates with 1.5 nm of native oxide layer by ALD at $300 \text{ }^\circ\text{C}$. Three distinct thicknesses of TiO₂ films, namely 11.27 nm (referred to as ALD10), 19.75 nm (referred to as ALD20), and 30.79 nm (referred to as ALD30), were achieved by using TiCl₄ as the metal-organic precursor and water as the oxidant for different numbers of ALD cycles (300, 540, 700 cycles, respectively). The thickness of the films was measured by spectroscopic ellipsometry. Each cycle's timing sequence was as follows: TiCl₄ exposure period of 140 ms, followed by N₂ purging (250 sccm) for 300 ms; exposure of water for 160 ms followed by N₂ purging (250 sccm) for 520 ms.

Synchrotron-Based X-ray Characterization. All the X-ray measurements were performed in the metrology laboratory of the Physikalisch-Technische Bundesanstalt (PTB) at the electron storage ring BESSY II of Helmholtz-Zentrum Berlin (HZB) in Berlin, Germany.³⁸ The GISAXS, GIXRF, and XRR experiments were performed at the four-crystal monochromator (FCM) beamline by using radiation with 6 keV photon energy. In GISAXS measurements, the incident beam with a spot size of $0.5 \text{ mm} \times 0.5 \text{ mm}$ impinged on the samples at grazing angle θ (0.70°), with an acquisition time of 30 s, at which the highest intensity of the diffraction pattern was observed. The elastically scattered waves were detected by an in-vacuum PILATUS 1 M hybrid pixel detector with $172 \mu\text{m} \times 172 \mu\text{m}$ pixel size,³² installed on a movable sledge and positioned at a distance of 5063 mm of distance from the samples. The GISAXS patterns were recorded on 10 different positions of each sample, integrating 20 measurements on each position. The uncertainty contributions of the pitch arise from the pixel size (0.1%), sample-detector distance (0.06%), photon energy E_{ph} (0.02%), and first-zero diffraction order distance (0.04%).³⁹

Reference-free quantification of the elemental mass concentration of Ti was performed by GIXRF measurements employing radio-metrically calibrated instrumentation⁴⁰ as previously detailed in the reference.⁴¹ The samples were placed in a 9-axis manipulator inside an ultrahigh-vacuum (UHV) chamber allowing the beam to impinge on the sample at grazing angles in the range from 0° to 2.5° . The selected incident photon energy allowed for the efficient excitation of the Ti-K fluorescence lines (XRF) while avoiding any fine structure modulation in the photoionization cross-section.³⁸

The XRF radiation is detected by a calibrated silicon drift detector (SDD) in terms of its detector response function^{42,43} and detection efficiency placed perpendicular to the incident X-ray beam direction and in the storage ring plane to minimize scattered radiation. The energy-dispersive detection of the SDD allows for the discrimination of the contribution from different elements via the characteristic energy of the XRF photons emitted from the samples, allowing, therefore, parallel processing during the quantification. A radiometrically calibrated photodiode is used to determine the incident photon flux. The count rates for the XRF line of interest were obtained by employing spectral deconvolution using the known detector response function for the different XRF and relevant background contributions. Afterward, to derive the number of emitted XRF photons for the

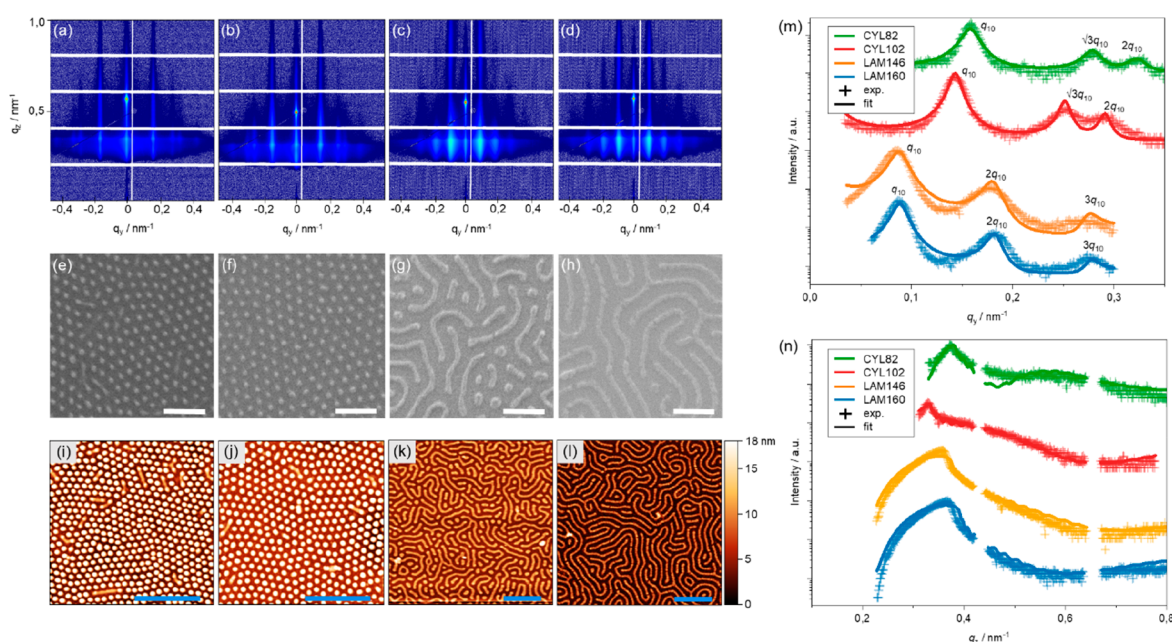


Figure 2. GISAXS patterns of TiO_2 nanostructures and relative top-view SEM images of (a, e) CYL82, (b, f) CYL102, (c, g) LAM146, and (d, h) LAM160. SEM scale bars are set to 200 nm. AFM micrographs on measurement fields $1 \times 1 \mu\text{m}^2$ of (i) CYL82 and (j) CYL102, and on measurement fields $2 \times 2 \mu\text{m}^2$ of (k) LAM146 and (l) LAM160 conducted in tapping mode in ambient conditions, scale bars are set to 400 nm. (m) GISAXS intensity profiles along q_y at a constant q_z of lamellar TiO_2 nanostructures ($q_z = 0.374 \text{ nm}^{-1}$ for CYL82; $q_z = 0.392 \text{ nm}^{-1}$ for CYL102; $q_z = 0.357 \text{ nm}^{-1}$ for LAM146; $q_z = 0.371 \text{ nm}^{-1}$ for LAM160) with relative curve fits calculated using BornAgain software. (n) Intensity profile along the first Bragg peak in q_z direction with relative curve fits calculated using BornAgain software ($q_y = 0.156 \text{ nm}^{-1}$ for CYL82; $q_y = 0.150 \text{ nm}^{-1}$ for CYL102; $q_y = 0.087 \text{ nm}^{-1}$ for LAM146; $q_y = 0.087 \text{ nm}^{-1}$ for LAM160). The incident beam and detector parameters along with the Bragg peak positions have been indexed manually.

different characteristic lines observed, the count rates were normalized to the incidence angle, incident photon flux, effective solid angle of detection, and the energy-dependent detection efficiency of the SDD. The titanium mass per unit area was extracted from the emitted XRF intensity of the Ti-K in an incidence angle range spanning from 1.25° to 2.5° . The uncertainty contributions arise from relative error of solid angle of detection (4%), relative error of incident photon flux (1.5%), relative error of detector efficiency (1.5%), relative error of Ti-K shell fluorescence yield (3.4%) and relative error of Ti-K shell photoionization cross section (5%). Absolute quantification of C on the infiltrated TiO_2 nanostructures was carried out at the plane grating monochromator (PGM) beamline at an incident photon energy $E_{\text{ph}} = 520 \text{ eV}$, which is just below the K-edge of the XRF such that secondary XRF excitation can be discarded. The uncertainty in the quantification of C depends on the uncertainties on the incident flux (1%), fluorescence yield (6%),⁴⁴ photoionization cross-section, (7.5%), the detector efficiency and spectral deconvolution (2.5%), the counting statistics and the solid angle of detection (15%) for a total uncertainty of 18%.

The XRR measurements were conducted in parallel to the GIXRF measurements, and the reflectivity $R(\theta)$ was measured by a photodiode in a $\theta-2\theta$ configuration. For the determination of the binding state, NEXAFS measurements on the infiltrated TiO_2 nanostructures were carried out at the PGM beamline in the soft X-ray regime ($E_{\text{ph}} < 1 \text{ keV}$) by varying the photon energy in the range of 450–480 eV and 525–550 eV to investigate the fine structure of the X-ray absorption of Ti $L_{2,3}$ -edge and O K -edge, respectively. The NEXAFS setup follows the same geometry as the GIXRF setup, and the measurements were realized in fluorescence mode, implying that a fluorescence spectrum is acquired for every photon energy by an SDD detector, and the relevant fluorescence count rates are subsequently normalized to the incident photon flux.

Scanning Probe and Electron Microscopies Characterization. TiO_2 nanostructures were monitored by an FEI Inspect-F field emission gun scanning electron microscope (FEG-SEM) using an Everhart–Thornley secondary electron detector (ETD). The SEM

images were then analyzed by using ImageJ software for their morphological characterization in terms of width and diameter. The samples were inspected by AFM in tapping mode with a Dimension Icon/Nanoscope V by Bruker. The scan sizes were $1 \times 1 \mu\text{m}^2$ and $2 \times 2 \mu\text{m}^2$. The height profiles were then extracted from the AFM micrographs using Gwyddion software.⁴⁵

Spectroscopic Ellipsometry Characterization. Spectroscopy ellipsometry (SE) was used in several steps of fabrication to control the thickness and optical constants of the polymeric films before and after the SIS process. The measurements were conducted using an alpha-SE ellipsometer (J.A. Wollam Co.) with a spectral range of 300 nm–900 nm at a fixed angle of 70° . The spectra analysis was performed using the CompleteEASE software, and the chosen model is discussed where appropriate in the Results and Discussion.

X-ray Photoelectron Spectroscopy. A PHI 5000 Versaprobe Scanning X-ray Photoelectron Spectrometer (Physical Electronics, Chanhassen, MN, USA) was used to perform the XPS analysis on the TiO_2 nanostructures obtained via the SIS process on the BCP templates. An Al anode, powered with a 15 kV voltage and 1 mA anode current, was used as a monochromatic Al $K\alpha$ X-ray source at 1486.6 eV. All samples, attached to the sample holder via conductive tape, were treated with a combined electron and Ar ion gun neutralizer system to decrease the electrical charging effect during the analysis and kept at a working pressure of 10^{-6} Pa . The TiO_2 nanostructure depth profiling was performed via layer-by-layer etching through argon plasma (2 kV) with 6 s time intervals. The XPS spectra were acquired after each etching step until the Si 2p signal was significantly higher than other elemental signals, indicating that the silicon substrate was reached. The atomic percent (at. %) of each species was found as a function of the time of etching, then converted to a depth of etching by taking advantage of the knowledge of the nanostructures thickness measured by AFM.

Table 1. Dimensional Results of TiO₂ Nanostructures from GISAXS, GIXRF-XRR, AFM, and SEM Data Analyses

Samples	$L_{0\text{GISAXS}}$ (nm)	ξ_{GISAXS} (nm)	d_{GISAXS} (nm)	w_{GISAXS} (nm)	h_{GISAXS} (nm)	d_{SEM} (nm)	w_{SEM} (nm)	h_{AFM} (nm)	$h_{\text{XRR-GIXRF}}$ (nm)
CYL82	44.1 ± 0.9	839 ± 210	19.0	/	19.4	23.0 ± 2.0	/	17.6 ± 2.1	15.7 ± 3.0
CYL102	48.8 ± 1.3	707 ± 177	23.3	/	14.0	24.5 ± 1.0	/	17.0 ± 2.2	15.6 ± 6.0
LAM146	68.2 ± 5.5	427 ± 107	/	34.0	6.9	/	34.6 ± 0.9	6.9 ± 2.6	6.8 ± 2.0
LAM160	67.4 ± 4.1	540 ± 105	/	34.0	7.3	/	34.1 ± 0.5	7.7 ± 2.0	7.3 ± 2.0

RESULTS AND DISCUSSION

GISAXS Geometrical Characterization. The first step toward the full characterization of the infiltrated BCPs relies on the assessment of the geometrical parameters of the form factor (i.e., height (h), width (w), or diameter (d)) and the structure factor (namely, the pitch (L_0) and correlation length (ξ)) of the small-angle scattering over the self-assembled microdomains. Statistical information on the morphology and relative size distribution can be directly yielded by traceable GISAXS measurements, thanks to the large area probing (square millimeters) determined by the footprint of the incident X-ray radiation at grazing angles.^{39,46} The GISAXS intensity patterns of model systems CYL82, CYL102, LAM146, and LAM160 are shown in Figure 2a–d, respectively.

The lamellar nanostructures' lateral periodicity L_0 can be extracted by assessing the distance of the first-order diffraction maximum to the zero-diffraction order following the expression:⁴⁷

$$L_0 = 2\pi m/q_y \quad (1)$$

where m is the order of the reflection, in which $m = 1$ for the first scattering peak, and q_y is the scattering peak position of the first diffraction order. In the case of cylindrical nanostructures the two-dimensional hexagonal lattice is expressed as⁴⁸

$$L_0 = 4\pi m/q_y \quad (2)$$

For both morphologies, the first-order intensity peak was found by tracing cuts along the q_y at a constant q_z as illustrated in Figure 2m. The q_z values on each GISAXS pattern were selected where the highest intensity was recorded ($q_z = 0.374 \text{ nm}^{-1}$ for CYL82; $q_z = 0.392 \text{ nm}^{-1}$ for CYL102; $q_z = 0.357 \text{ nm}^{-1}$ for LAM146; and $q_z = 0.371 \text{ nm}^{-1}$ for LAM160). In samples LAM146 and LAM160, the characteristic GISAXS intensity profiles consist of peaks multiple of the first-order typical of a lamellar pattern. For cylindrical samples (CYL82 and CYL102) the peak positions are scaled following the ratio $1:\sqrt{3}:2:\sqrt{7}$ typical of a 2D hexagonal lattice.⁴⁹

The L_0 of cylindrical samples, (44.1 ± 0.9) nm for CYL82 and (48.8 ± 1.3) nm for CYL102, exhibit an increase along with the M_w and are in good agreement with those found in literature in the strong segregation limit (SSL),^{50,51} whereas an unexpected opposite trend was observed for lamellar samples ($L_0 = 68.2 \pm 5.5 \text{ nm}$ for LAM146 and $L_0 = 67.4 \pm 4.1 \text{ nm}$ for LAM160). Such a discrepancy can be related to the higher polydispersity index (PDI) = 1.20 of the sample LAM146, which also reflects in a broader pitch dispersion.

Further analysis of the q_{10} intensity peak can be applied to extract information about the long-range lateral ordering of the nanostructures. To this end, the Scherrer formula,⁵² relates the full width at half-maximum of the first Bragg order peak to the average grain size of self-assembled patterns, providing direct information on ξ .⁴⁷ As reported in Table 1, all samples,

whether lamellar or cylindrical morphologies, exhibit high ξ values exceeding 400 nm. However, two distinct variations on the ξ can be observed for lamellar (LAM146 and LAM160) and cylindrical (CYL82 and CYL102) nanostructures. Both sets of samples underwent two different self-assembly processing parameters, respectively. Lamellar BCPs were annealed by RTP at 230 °C for 600 s, whereas the cylindrical samples were thermally treated in RTP at 190 °C for 450 s. Higher M_w lamellar sample LAM160 shows a higher ξ value of (540 ± 105) nm when compared to a lower M_w LAM146 that showed a ξ value of (427 ± 107) nm, thus indicating more favorable thermal annealing conditions to promote the self-assembly process of high M_w BCPs. On the contrary, in cylindrical samples CYL82 and CYL102, by monitoring the ξ evolution, one can notice an opposite trend to the lamellar ones. Under these processing conditions, thermal annealing promotes an increased nanostructure ordering for lower M_w BCPs CYL82 of (839 ± 210) nm compared to lower M_w BCPs CYL102 with a value of (707 ± 177) nm. It must be noted, however, that the overall high confidence intervals lead to no significant differences among the ξ values due to the overlap of the relative error bars represented as one standard deviation (1σ) due to uncertainty in the fit.⁵³

All the parameters defining the nanostructure's shape (i.e., height, cylinder diameter, and lamellae width) were extracted by modeling and least-squares fitting the GISAXS patterns using the distorted-wave Born approximation, implemented in the software BornAgain.⁵⁴ This software allows for a simplistic description of arbitrary form factors that can be selected from a catalog and parametrized, resulting in an overall increased computational speed for the computing of GISAXS patterns. The GISAXS patterns were calculated from scattering form functions of perfectly straight cylinders on a hexagonal lattice for the description of CYL82 and CYL102 and scattering form factor of a box (cuboid) for LAM146 and LAM160 at the same incident X-ray wavelength used in the experiment. A good agreement of the fitting of the profile cuts along q_y at a constant q_z (Figure 2m) and of the intensity profile along the first Bragg peak in q_z direction (Figure 2n) was obtained for low χ^2 values after matching the length scales of the peak positions in q_y . The results reveal the geometrical parameters, reported in Table 1, such as the diameters of cylindrical TiO₂ nanostructures (19.0 nm for CYL82 and 23.3 nm for CYL102) and the width of lamellar features (34.0 nm for both samples LAM146 and LAM160), as well as the nanostructure heights (19.4 nm for CYL82; 14.0 nm for CYL102; 6.9 nm for LAM146 and 7.3 nm for LAM160). For simplicity, the values of all of the geometrical parameters extracted from the GISAXS analysis are summarized in Table 1.

Complementary Dimensional Characterization. The morphological analysis was complemented by SEM and AFM investigation. The nanostructures' width and diameter determinations were performed by a two-dimensional Fourier transform and radial averaging of representative SEM images collected in random locations and at different magnifications

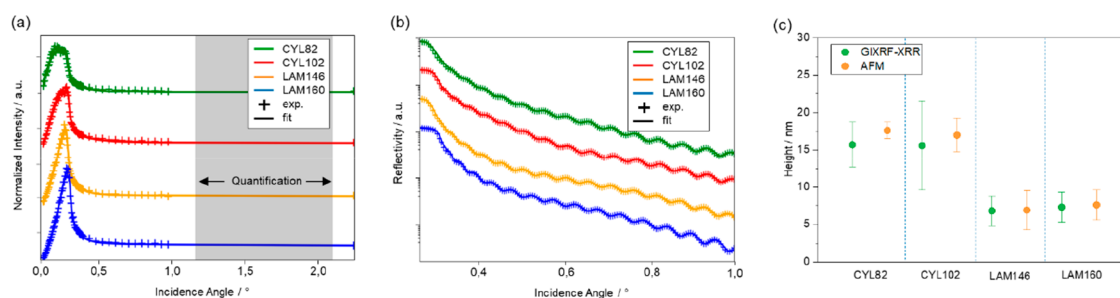


Figure 3. (a) Ti–K GIXRF spectra for the infiltrated TiO₂ nanostructures measured at FCM beamline with a 6 keV incident beam energy (the data in the angular range above the critical angle for total external reflection highlighted in gray, can be used for the quantification of the element of interest) and (b) relative reflectivity curves. (c) Comparison of the infiltrated TiO₂ height values obtained by AFM measurements and GIXRF-XRR modeling. Confidence intervals (1σ) of the GIXRF-XRR hybrid model are derived from Markov chain Monte Carlo analysis.⁵⁸

over the entire sample surface and expressed with a relative standard deviation of the mean peak position. The second-order radial averaging fitting provides information on the typical lateral dimensions of the nanostructures that are reported in Table 1. The cylindrical samples show a variation of d as a function of the M_w , from (23.0 ± 2.0) nm for CYL82 to (24.5 ± 1.0) nm for CYL102. Whereas the w of TiO₂ lamellar features is (34.6 ± 0.9) nm for LAM146 and (34.1 ± 0.5) nm for LAM160. The heights of the nanostructures determined by AFM measurements (Figure 2i-l) reveal dissimilar values for lamellar and cylindrical morphology. The lamellar nanostructures are characterized by a reduced height of (6.9 ± 2.6) nm for LAM146 and (7.7 ± 2.0) nm for LAM160 when compared to the cylindrical ones with nanofeature heights of (17.6 ± 2.1) nm for CYL82 and (17.0 ± 2.0) nm for CYL102. Evidence that the AFM probe was able to reach the substrate surface in between the nanometric features is provided by additional AFM scans of sample LAM160 in Figure S3, revealing small roughness on the flat area. All samples were fabricated following the same spin-coating parameters, therefore depositing the same polymeric film thickness of nominally 35 nm. Moreover, all of the samples underwent the same infiltration conditions, preventing therefore any process-to-process variation of metal–organic precursor concentration inside the ALD chamber. Therefore, the increased height of the cylindrical features compared to the lamellar nanostructures can be attributed to the lower PMMA volume fraction ($\sim 30\%$) when compared to the lamellar ones ($\sim 50\%$). The reduced volume fraction of the reactive polymeric phase (PMMA) in a hexagonally packed cylindrical configuration imposes lateral restrictions on the growth of inorganic material. Consequently, the metal oxide deposition distributes along the z -axis, resulting in an overall increased nanostructures' height.

Material Quantification. Absolute quantification of the mass thickness per unit area of infiltrated material can be provided by reference-free GIXRF,^{38,41,55} applied at incidence angles above the critical angle of total reflection.⁴⁰ Figure 3a illustrates the normalized incident angle-dependent intensity profiles of Ti–K of the infiltrated TiO₂ nanostructures. The GIXRF spectra are characterized by modulations of the fluorescence intensity at incidence angles in the range from 0.0° to 0.5° due to X-ray standing wave (XSW) field interactions with the nanostructures for all the analyzed samples.⁵⁶ At incidence angles higher than the critical angle for total external reflection, a traceable reference-free quantification of the titanium mass thickness per unit area⁵⁷ can be performed with a good knowledge of the uncertainty

contributions of the instrumental parameters described in the Experimental Section.

Table 2 shows the Ti mass thickness per unit area quantified by GIXRF, which varies in the range from (263 ± 22) to $(302$

Table 2. Absolute Ti and C Mass Thicknesses Per Unit Area and Related Uncertainties

Samples	Ti mass thickness (ng/cm ²)	C mass thickness (ng/cm ²)
CYL82	263 ± 22	300 ± 54
CYL102	282 ± 23	365 ± 66
LAM146	264 ± 22	378 ± 69
LAM160	302 ± 25	354 ± 64

$\pm 25)$ ng/cm² for both lamellar and cylindrical samples, indicating that differences occur in the mass uptake of TiO₂ upon sequential infiltration synthesis depending on the M_w of the BCP template. However, the absolute quantification of Ti remains consistent with the known infiltration mechanism in PS and PMMA.⁵⁹

Moreover, the simultaneous execution of GIXRF (Figure 3a) and XRR measurements (Figure 3b) allows for the combined modeling of the fluorescence and reflectivity data, to derive the depth profiles (Figure S4a) of the relative concentration of the target element, which is Ti in this case.⁶⁰ GIXRF-XRR modeling revealed height values of (15.7 ± 3.0) for CYL82, (15.6 ± 6.0) for CYL102, (6.8 ± 2.0) for LAM146 and (7.3 ± 2.0) for LAM160. These results are in good agreement with the experimental measurements obtained by AFM and consistent within the confidence intervals (Figure 3c).⁵⁸ On the other hand, discrepancies on the elemental distribution arise when compared to XPS analysis combined with a step-by-step *in situ* ion etching, suggesting that further investigation is needed (Figure S4b–e).

Additional XRF measurements were performed for the quantification of residual C at an incidence angle of 15° and incident photon energy of 520 eV (Table 2).⁶¹ The measurements reveal a noticeable amount of C, in the range from (300 ± 54) to (378 ± 69) ng/cm². The overall high quantity of C, still present on the nanostructures, can be attributed to the incomplete removal of all of the organic material infused with TiO₂ after subsequent Ar plasma treatment. Although being in isotropic conditions, Ar plasma does not chemically react with the polymeric matrix, thus the etching process is reduced to a physical sputtering that leads to a significant graphitization of the polymeric template. This issue might be overcome by O₂ plasma etching processes in which the additional chemical sputtering effects of O₂ to the

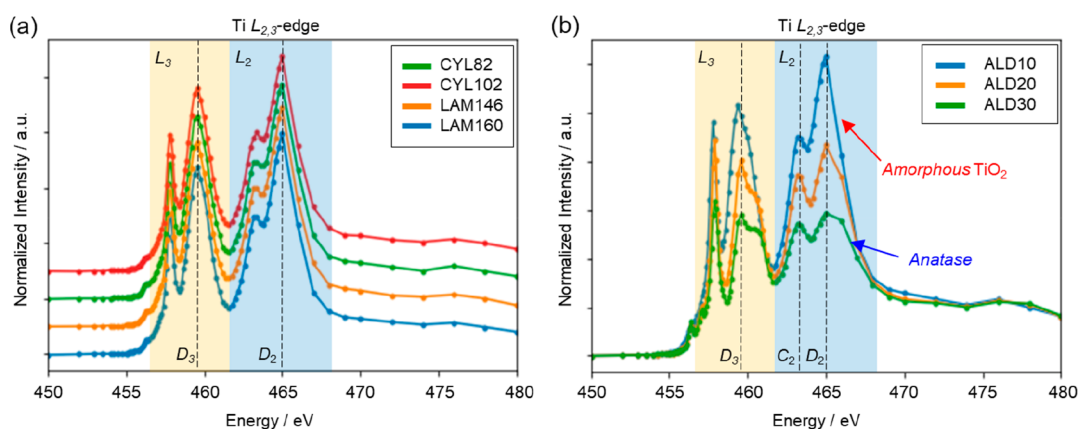


Figure 4. Ti $L_{2,3}$ -edge spectra of (a) TiO₂ fabricated by sequential infiltration synthesis (LAM146, LAM160, CYL82, and CYL102) and (b) TiO₂ thin films fabricated ALD with different thicknesses (nominally 10, 20, and 30 nm).

physical one, determine rapid oxidation and ion-induced desorption that would prevent the formation of residual C.^{62,63}

Chemical and Compositional Characterization. The comprehensive characterization of infiltrated TiO₂ requires the assessment of the effective composition and chemical speciation. To this end, near-edge X-ray absorption fine structure (NEXAFS) measurements ensure the identification of chemical valence states. NEXAFS measurements on the infiltrated TiO₂ nanostructures were carried out in the soft X-ray regime ($E_{\text{ph}} < 1$ keV) by varying the photon energy in the range of 450–480 eV at an incidence angle of 30° to investigate the fine structure of the X-ray absorption of Ti $L_{2,3}$ -edge.⁶⁴ The results are reported in Figure 4a where the peak positions of the four curves related to the infiltrated samples perfectly overlap each other, suggesting that there are no differences in the chemical binding states. The fine structure is divided into two main groups separated by ~5.5 eV related to the L_3 and L_2 -edges respectively. The material under consideration exhibits a very broad L_2 -edge, dominated by a D_2 peak along with a broadened D_3 peak in the L_3 -edge. A comparison of these spectra to those reported in literature⁶⁵ clearly suggests that the infiltrated TiO₂ is amorphous. Moreover, the absence of any peaks related to other Ti species indicates complete oxidation of TiO₂, confirming the 1:2 stoichiometry of Ti and O. Additional XPS spectra acquired on the surface of the four TiO₂ nanostructured samples confirm that the top surface is characterized by stoichiometric TiO₂, as shown in Figure S5. However, the XPS depth profiles complement the NEXAFS surface analysis since, with progressive etching steps, the Ti 2p XPS signal reveals a nonstoichiometric TiO₂.

As a comparison to the samples fabricated by SIS, three TiO₂ thin films deposited by conventional ALD with three different thicknesses (nominally 10, 20, and 30 nm) were measured at the same experimental conditions. Figure 4b shows that in TiO₂ thin layers fabricated by ALD, the peak intensities, positions, and widths follow a completely different evolution along the film thickness. In thicker ALD layers of 30 nm, the C_2 and D_2 peaks in L_2 -edge spectra show a different intensity ratio, typical of the anatase polymorph, confirmed also by the L_3 -edge that splits into two peaks, predominantly dominated by D_3 . By reducing the TiO₂ to 20 and 10 nm, an overall progressive evolution of the peak intensities is noted. The reduced film thickness induces variations of peak intensity ratios in the L_2 and L_3 -edge regions with a progressive shift of

D_2 and D_3 peaks to lower energies along with a substantial increase in intensity. This behavior can be attributed to a gradual amorphization of the anatase crystalline phase for reduced film thicknesses. Similar behavior of the TiO₂ thin films along with reduced thickness is monitored also by O K -edge NEXAFS spectra in a photon energy range of 525–550 eV as shown in Figure S6a. Here, the significant distance reduction between C_0 and E_0 peaks is caused by a shift of E_0 to lower energies accompanied by a broadening of all of the peaks in the spectra. A clear confirmation of the progressive amorphization process of films with reduced thicknesses is provided by spectroscopic ellipsometry (SE) to monitor the refractive indices. The refractive indices were extracted from SE measurements by fitting the experimental data to a Cauchy model. The refractive indices exhibit a linear increase for increasing TiO₂ film thicknesses (Figure S6b). For 30 nm thin films of TiO₂, a refractive index of 2.53 at 550 nm is in good agreement with the tabulated value of a bulk anatase polymorph ($n = 2.65$ at 550 nm)⁶⁶ and consistent with previous works by Niilisk et al.,⁶⁷ where TiO₂ grown by TiCl₄-H₂O ALD process begins to crystallize at a growth temperature of approximately 150 °C and at a critical thickness of around 15 nm. On the other hand, reduced film thicknesses of 20 and 10 nm thin films correspond to lower refractive indices ($n = 2.46$ and 2.36 at 550 nm, respectively) when compared to a crystalline TiO₂, therefore related to an amorphous TiO₂ phase. By taking advantage of the direct correlation between the refractive index and mass density values for TiO₂ established by Otterman and Bange,⁶⁸

$$\rho = 2.83n - 3.27 \quad (3)$$

where ρ is the mass density and n the refractive index at 550 nm, the calculated mass density for a 30 nm thin TiO₂ layer is 3.9 g/cm³, matching the reported mass density of bulk anatase.⁶⁹ The reduced refractive indices of 10 and 20 nm thin films result also in a lower mass density of 3.4 g/cm³ and 3.7 g/cm³, respectively, in accordance with mass densities that typically range from 2.9 g/cm³ to 3.9 g/cm³ for amorphous TiO₂.⁷⁰

Validation by Spectroscopic Ellipsometry. A parallel assessment of the optical properties of infiltrated TiO₂ nanostructures was performed by SE measurements. This method allows for gaining information on the effective refractive indices of the synthesized materials by taking advantage of the geometrical parameters of the nanostructures

to parametrize an effective medium approximation (EMA) model. The EMA model employed in these analyses consists of a mixture of materials composed of amorphous TiO_2 and PMMA. The chemical similarities in the binding states of infiltrated material and 10 nm thin films of TiO_2 deposited by ALD, as confirmed by NEXAFS analyses in Figure 4a,b allow for the implementation of the 10 nm thin film and its related optical constants as a starting material with progressively reduced refractive index along with increasing PMMA volume fraction. The optical constants of sample ALD10 were extracted by fitting its ellipsometry data to a Cauchy model. Whereas the parametrization of the EMA model was performed by implementing the geometrical results obtained by two different sets of analytical methods described above (synchrotron-based and lab-scale), independently. Specifically, the parametrization of the EMA model was performed by inserting the geometrical parameters determined by synchrotron-based measurements such as covered surface area determined by L_0 and w or d from GISAXS measurements and nanostructures' height from GIXRF-XRR modeling. Whereas the parametrization of the EMA model with geometrical parameters from lab-scale measurements was performed by inserting the covered surface area determined by L_0 and w or d from SEM analysis and nanostructures' height from AFM measurements.

Figure 5 shows that the refractive indices are overall reduced when compared to a 10 nm thick TiO_2 deposited by ALD ($n =$

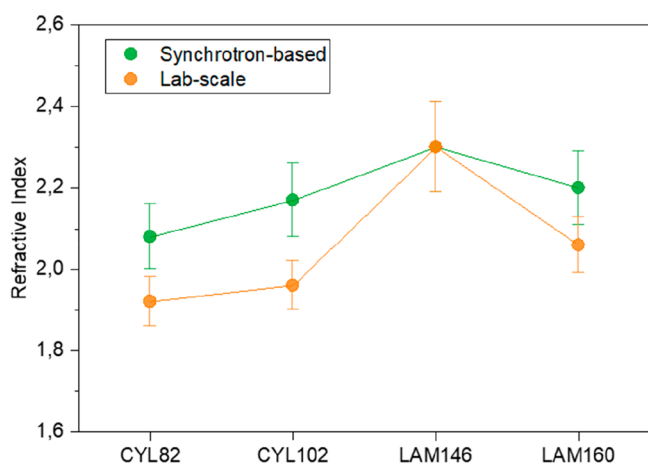


Figure 5. Refractive indices extracted from SE measurements of infiltrated TiO_2 samples. The error bars represent the standard deviation associated with the refractive indices over the entire Vis range (400–900 nm). The refractive indices were determined by fitting the experimental measurements to the Bruggeman EMA model. The parametrization of the model was performed by inserting the geometrical parameters determined by synchrotron-based measurements (GISAXS and GIXRF-XRR indicated with the green spheres) and lab-based measurements (SEM and AFM indicated with orange spheres). The EMA model consists of a mixture of materials composed of amorphous TiO_2 , whose optical constants were extracted from SE measurements of TiO_2 thin film fabricated by conventional ALD (ALD10) and PMMA.

2.36), irrespective of the data employed for the parametrization of the EMA model. A slight increase of the refractive index along with the M_w of the starting BCP template is noted for cylindrical nanostructures when compared to the lamellar ones in both synchrotron-based and lab-scale results. The dependency of the refractive indices with respect to the

PMMA volume fraction in the TiO_2 /PMMA composite indicates the presence of high quantities of residual PMMA inside the amorphous infiltrated TiO_2 from ~20% up to almost 50% in volume (Figure S7). However, substantial differences of the refractive indices emerged when extracted from the two distinct sets of analytical methods. In particular, lab-scale methods yielded underestimated values (orange spheres) when compared to those extracted from traceable synchrotron-based measurements (green spheres), representing clear evidence to the necessity to define metrological routes to provide traceability to the measurements and more reliable results.

CONCLUSIONS

In summary, we have reported a hybrid metrology approach applied to inorganic nanostructures with different morphologies that is useful to support the development of optical metasurfaces. Numerical calculations revealed that the refractive indices of the polymer/ TiO_2 nanostructures sensibly influence the resulting optical functionalities of optical metasurfaces. SIS was employed to engineer TiO_2 nanostructures with distinct morphologies (cylinders and lamellae) and dimensions. These nanostructures served as model systems for elucidating the intricate interplay between the chemical composition and geometric attributes of the synthesized material and their resulting optical properties. Our investigation integrated state-of-the-art synchrotron-based analytical techniques alongside conventional laboratory-scale equipment following a hybrid metrology approach. Geometric characterization of the model systems, performed by GISAXS, SEM, and AFM, enabled the precise determination of dimensional parameters (L_0 , h , w , d). Absolute mass thickness per unit area of Ti with relative in-depth profile distribution obtained from the modeling of GIXRF angular profiles and XRR was complemented by XPS analysis combined with a step-by-step *in situ* ion etching. NEXAFS analyses unveiled amorphous stoichiometric chemical speciation at the top surface of the TiO_2 nanostructures, while XPS analysis disclosed a non-stoichiometric TiO_2 composition within their inner regions. These insights, obtained through complementary analytical techniques, informed model-assisted spectroscopic ellipsometry to determine the effective refractive index of the SIS-fabricated TiO_2 nanostructures. The refractive indices showed reduced values compared to those of crystalline TiO_2 , also revealing their dependency over the BCP template's morphology and M_w . Significant differences when comparing refractive indices extracted from the two distinct sets analytical methods. In particular, lab-scale methods yielded underestimated values when compared to those extracted from traceable synchrotron-based measurements. This underscores the necessity of defining metrological pathways to ensure measurement traceability and enhance result reliability. The great flexibility offered by SIS, in terms of control on the composition and dimensions of the features, allows us to envision its application for the development of a high throughput metrology at the nanoscale of functional materials with controlled optical properties, as well as reference materials.

Precise characterization and a comprehensive understanding of the chemical and physical properties of infiltrated polymeric materials are pivotal for advancing the sophistication of photonic metamaterials. The generic attributes of hybrid metrology allow us to foresee this application not only limited to photonics but also as a universal method that can be expanded also to the development, in a “materials by design”

approach, of next-generation electronic devices and energy storage systems.

■ ASSOCIATED CONTENT

Data Availability Statement

The data underlying this study are openly available in Zenodo at 10.5281/zenodo.10182956.

SI Supporting Information

The Supporting Information is available free of charge at <https://pubs.acs.org/doi/10.1021/acsami.3c13923>.

Additional experimental details are available, concerning false color maps of the computed Purcell factor, additional AFM and GIXRF-XRR depth profiles, XPS and NEXAFS O *K*-edge spectra, and the results of the refractive indices measured by spectroscopic ellipsometry (PDF)

■ AUTHOR INFORMATION

Corresponding Authors

Irdi Murataj – *Advanced Materials and Life Science Division, Istituto Nazionale Ricerca Metrologica (INRiM), 10135 Torino, Italy; Dipartimento di Scienza Applicata e Tecnologia, Politecnico di Torino, 10129 Torino, Italy;* orcid.org/0000-0001-9529-7959; Email: irdi.murataj@polito.it

Federico Ferrarese Lupi – *Advanced Materials and Life Science Division, Istituto Nazionale Ricerca Metrologica (INRiM), 10135 Torino, Italy;* orcid.org/0000-0002-1055-8839; Email: f.ferrareseilupi@inrim.it

Authors

Angelo Angelini – *Advanced Materials and Life Science Division, Istituto Nazionale Ricerca Metrologica (INRiM), 10135 Torino, Italy*

Eleonora Cara – *Advanced Materials and Life Science Division, Istituto Nazionale Ricerca Metrologica (INRiM), 10135 Torino, Italy;* orcid.org/0000-0002-5981-9569

Samuele Porro – *Dipartimento di Scienza Applicata e Tecnologia, Politecnico di Torino, 10129 Torino, Italy;* orcid.org/0000-0003-3093-6099

Burkhard Beckhoff – *Physikalisch-Technische Bundesanstalt (PTB), 10587 Berlin, Germany*

Yves Kayser – *Physikalisch-Technische Bundesanstalt (PTB), 10587 Berlin, Germany; Present Address: Y.K. Max Planck Institute for Chemical Energy Conversion, Stiftstr. 34–36, 45470 Mülheim an der Ruhr, Germany;* orcid.org/0000-0002-0301-2918

Philipp Hönicke – *Physikalisch-Technische Bundesanstalt (PTB), 10587 Berlin, Germany*

Richard Ciesielski – *Physikalisch-Technische Bundesanstalt (PTB), 10587 Berlin, Germany;* orcid.org/0000-0002-7780-2904

Christian Gollwitzer – *Physikalisch-Technische Bundesanstalt (PTB), 10587 Berlin, Germany;* orcid.org/0000-0002-6437-8825

Victor Soltwisch – *Physikalisch-Technische Bundesanstalt (PTB), 10587 Berlin, Germany*

Francesc Perez-Murano – *IMB-CNM CSIC, Carrer dels Til·lers, 08193 Barcelona, Spain*

Marta Fernandez-Regulez – *IMB-CNM CSIC, Carrer dels Til·lers, 08193 Barcelona, Spain*

Stefano Carignano – *ICCUB, Universitat de Barcelona, 08028 Barcelona, Spain*

Luca Boarino – *Advanced Materials and Life Science Division, Istituto Nazionale Ricerca Metrologica (INRiM), 10135 Torino, Italy;* orcid.org/0000-0002-1221-2591

Micaela Castellino – *Dipartimento di Scienza Applicata e Tecnologia, Politecnico di Torino, 10129 Torino, Italy;* orcid.org/0000-0002-1393-4043

Complete contact information is available at: <https://pubs.acs.org/doi/10.1021/acsami.3c13923>

Author Contributions

I.M., F.F.L., and B.B. conceptualized the idea. I.M., F.F.L., and E.C. performed sample preparation and data analysis. A.A. performed simulations, and Y.K., P.H., and I.M. performed GIXRF, XRR, and NEXAFS characterization and data analysis. I.M., F.F.L., R.C., C.G., V.S., and S.C. performed GISAXS characterization and data analysis, and M.C. performed XPS measurements. L.B. and B.B. provided funding and laboratory equipment. S.P. provided laboratory equipment. All authors contributed to writing and/or revising the manuscript.

Funding

Project funded by the European Union—NextGenerationEU under the National Recovery and Resilience Plan (NRRP), Mission 04 Component 2 Investment 3.1|Project Code: IR0000027—CUP: B33C22000710006—iENTRANCE@ENL: Infrastructure for Energy TRAnSition aNd Circular Economy @EuroNanoLab. Part of this work was supported by the European project 21GRD01 OpMetBat. The project has received funding from the European Partnership on Metrology, cofinanced from the European Union's Horizon Europe Research and Innovation Programme, and by Participating States. Part of this work has been carried out in the framework of the EMPIR Researcher Mobility Grant 20FUN06-RMG2. Part of this work has been carried out at Nanofacility Piemonte, a laboratory supported by the “Compagnia di San Paolo” Foundation, and at the QR Laboratories, INRiM. This project has received funding from the European Union's Horizon 2020 research and innovation program under grant agreement No 101007417 having benefitted from the access provided by IMB-CNM CSIC (Spain) within the framework of the NFFA-Europe Pilot Transnational Access Activity, proposal ID-090. In particular, the authors thank Xavier Borrisé Nogué, Albert Guerrero Barbero, and Miguel Zabala García of IMB-CNM CSIC for their kind support.

Notes

The authors declare no competing financial interest.

■ REFERENCES

- (1) Li, L.; Zhao, H.; Liu, C.; Li, L.; Cui, T. J. Intelligent Metasurfaces: Control, Communication and Computing. *eLight* **2022**, *2* (1), 7.
- (2) Neshev, D. N.; Miroshnichenko, A. E. Enabling Smart Vision with Metasurfaces. *Nat. Photonics* **2023**, *17*, 26.
- (3) Pitruzzello, G. Metaoptics for the Consumer Market. *Nat. Photonics* **2023**, *17* (1), 6–7.
- (4) Pile, D. Metamaterials for the Masses. *Nat. Photonics* **2023**, *17* (1), 2–3.
- (5) Saha, S.; Cano-Garcia, H.; Sotiriou, I.; Lipscombe, O.; Gouzouasis, I.; Koutsoupidou, M.; Palikaras, G.; Mackenzie, R.; Reeve, T.; Kosmas, P.; Kallos, E. A Glucose Sensing System Based on Transmission Measurements at Millimetre Waves Using Micro Strip Patch Antennas. *Sci. Rep* **2017**, *7* (1), 1–11.

- (6) Gu, T.; Kim, H. J.; Rivero-Baleine, C.; Hu, J. Reconfigurable Metasurfaces towards Commercial Success. *Nat. Photonics* **2023**, *17* (1), 48–58.
- (7) Gemini dual pattern projectors. <https://metalenz.com/gemini-dual-pattern-projectors/> (accessed 2023-11-07).
- (8) Metalenz and STMicroelectronics deliver world's first optical metasurface technology for consumer electronics devices. <https://newsroom.st.com/media-center/press-item.html/t4458.html> (accessed 2023-11-07).
- (9) Lume Pad 3D Lightfield Tablet. <https://www.leiainc.com/> (accessed 2023-11-07).
- (10) Pile, D. Metasurfaces Get Smart. *Nat. Photonics* **2023**, *17* (1), 4–5.
- (11) META's technology solutions. <https://metamaterial.com/industries/energy/> (accessed 2023-11-07).
- (12) Yu, N.; Capasso, F. Flat Optics with Designer Metasurfaces. *Nat. Mater.* **2014**, *13* (2), 139–150.
- (13) Miller, D. A. B. Why Optics Needs Thickness. *Science* (1979) **2023**, *379* (6627), 41–45.
- (14) Sun, S.; Yang, W.; Zhang, C.; Jing, J.; Gao, Y.; Yu, X.; Song, Q.; Xiao, S. Real-Time Tunable Colors from Microfluidic Reconfigurable All-Dielectric Metasurfaces. *ACS Nano* **2018**, *12* (3), 2151–2159.
- (15) Huang, Y.; Xu, H.; Lu, Y.; Chen, Y. All-Dielectric Metasurface for Achieving Perfect Reflection at Visible Wavelengths. *J. Phys. Chem. C* **2018**, *122* (5), 2990–2996.
- (16) Poddubny, A.; Iorsh, I.; Belov, P.; Kivshar, Y. Hyperbolic Metamaterials. *Nat. Photonics* **2013**, *7* (12), 948–957.
- (17) Lee, D.; So, S.; Hu, G.; Kim, M.; Badloe, T.; Cho, H.; Kim, J.; Kim, H.; Qiu, C.-W.; Rho, J. Hyperbolic Metamaterials: Fusing Artificial Structures to Natural 2D Materials. *eLight* **2022**, *2* (1), 1–23.
- (18) Kapitanova, P. V.; Ginzburg, P.; Rodríguez-Fortuño, F. J.; Filonov, D. S.; Voroshilov, P. M.; Belov, P. A.; Poddubny, A. N.; Kivshar, Y. S.; Wurtz, G. A.; Zayats, A. V. Photonic Spin Hall Effect in Hyperbolic Metamaterials for Polarization-Controlled Routing of Subwavelength Modes. *Nat. Commun.* **2014**, *5* (1), 3226.
- (19) Cho, H.; Yang, Y.; Lee, D.; So, S.; Rho, J. Experimental Demonstration of Broadband Negative Refraction at Visible Frequencies by Critical Layer Thickness Analysis in a Vertical Hyperbolic Metamaterial. *Nanophotonics* **2021**, *10* (15), 3871–3877.
- (20) High, A. A.; Devlin, R. C.; Dibos, A.; Polking, M.; Wild, D. S.; Percel, J.; De Leon, N. P.; Lukin, M. D.; Park, H. Visible-Frequency Hyperbolic Metasurface. *Nature* **2015**, *522* (7555), 192–196.
- (21) Lu, D.; Kan, J. J.; Fullerton, E. E.; Liu, Z. Enhancing Spontaneous Emission Rates of Molecules Using Nanopatterned Multilayer Hyperbolic Metamaterials. *Nat. Nanotechnol.* **2014**, *9* (1), 48–53.
- (22) Sreekanth, K. V.; Krishna, K. H.; De Luca, A.; Strangi, G. Large Spontaneous Emission Rate Enhancement in Grating Coupled Hyperbolic Metamaterials. *Sci. Rep.* **2014**, *4*, 6340.
- (23) Shomrat, N.; Chirko, K.; Weisbord, I.; Avniel, Y.; Khristo, S.; Nessim, D.; Litman, A.; Segal-Peretz, T. Development and Evaluation of Three-Dimensional Metrology of Nanopatterns Using Electron Microscopy. *Journal of Micro/Nanopatterning, Materials and Metrology* **2022**, *21* (2), No. 021202.
- (24) Weisbord, I.; Segal-Peretz, T. Revealing the 3D Structure of Block Copolymers with Electron Microscopy: Current Status and Future Directions. *ACS Appl. Mater. Interfaces* **2023**, DOI: 10.1021/acsami.3c02956.
- (25) Simon, A.; Zhang, Z.; Abetz, C.; Abetz, V.; Segal-Peretz, T. Atomic Layer Deposition Enables Multi-Modal Three-Dimensional Electron Microscopy of Isoporous Membranes. *Nanoscale* **2023**, *15* (7), 3219–3229.
- (26) Lee, S.; Subramanian, A.; Tiwale, N.; Kisslinger, K.; Mumtaz, M.; Shi, L.-Y.; Aissou, K.; Nam, C.-Y.; Ross, C. A. Resolving Triblock Terpolymer Morphologies by Vapor-Phase Infiltration. *Chem. Mater.* **2020**, *32* (12), 5309–5316.
- (27) He, X.; Waldman, R. Z.; Mandia, D. J.; Jeon, N.; Zaluzec, N. J.; Borkiewicz, O. J.; Ruett, U.; Darling, S. B.; Martinson, A. B. F.; Tiede, D. M. Resolving the Atomic Structure of Sequential Infiltration Synthesis Derived Inorganic Clusters. *ACS Nano* **2020**, *14* (11), 14846–14860.
- (28) Cara, E.; Murataj, I.; Milano, G.; De Leo, N.; Boarino, L.; Ferrarese Lupi, F. Recent Advances in Sequential Infiltration Synthesis (SIS) of Block Copolymers (BCPs). *Nanomaterials* **2021**, *11* (4), 994.
- (29) Peng, Q.; Tseng, Y. C.; Darling, S. B.; Elam, J. W. Nanoscopic Patterned Materials with Tunable Dimensions via Atomic Layer Deposition on Block Copolymers. *Adv. Mater.* **2010**, *22* (45), 5129–5133.
- (30) Russell, S. T.; Bae, S.; Subramanian, A.; Tiwale, N.; Doerk, G.; Nam, C. Y.; Fukuto, M.; Yager, K. G. Priming Self-Assembly Pathways by Stacking Block Copolymers. *Nat. Commun.* **2022**, *13* (1), No. 6947, DOI: 10.1038/s41467-022-34729-0.
- (31) Berman, D.; Guha, S.; Lee, B.; Elam, J. W.; Darling, S. B.; Shevchenko, E. V. Sequential Infiltration Synthesis for the Design of Low Refractive Index Surface Coatings with Controllable Thickness. *ACS Nano* **2017**, *11* (3), 2521–2530.
- (32) Waldman, R. Z.; Mandia, D. J.; Yanguas-Gil, A.; Martinson, A. B. F.; Elam, J. W.; Darling, S. B. The Chemical Physics of Sequential Infiltration Synthesis—A Thermodynamic and Kinetic Perspective. *J. Chem. Phys.* **2019**, *151* (19), No. 190901.
- (33) Murataj, I.; Channab, M.; Cara, E.; Pirri, C. F.; Boarino, L.; Angelini, A.; Ferrarese Lupi, F. Hyperbolic Metamaterials via Hierarchical Block Copolymer Nanostructures. *Adv. Opt. Mater.* **2021**, *9* (7), 1–9.
- (34) Beckhoff, B. Traceable Characterization of Nanomaterials by X-Ray Spectrometry Using Calibrated Instrumentation. *Nanomaterials* **2022**, *12* (13), 2255.
- (35) Sparnacci, K.; Antonioli, D.; Perego, M.; Giammaria, T. J.; Seguni, G.; Ferrarese Lupi, F.; Zuccheri, G.; Gianotti, V.; Laus, M. High Temperature Surface Neutralization Process with Random Copolymers for Block Copolymer Self-Assembly. *Polym. Int.* **2017**, *66* (3), 459–467.
- (36) Ferrarese Lupi, F.; Murataj, I.; Celegato, F.; Angelini, A.; Frascella, F.; Chiarcos, R.; Antonioli, D.; Gianotti, V.; Tiberto, P.; Pirri, C. F.; Boarino, L.; Laus, M. Tailored and Guided Dewetting of Block Copolymer/Homopolymer Blends. *Macromolecules* **2020**, *53*, 7207.
- (37) Shin, D. O.; Mun, J. H.; Hwang, G. T.; Yoon, J. M.; Kim, J. Y.; Yun, J. M.; Yang, Y. B.; Oh, Y.; Lee, J. Y.; Shin, J.; Lee, K. J.; Park, S.; Kim, J. U.; Kim, S. O. Multicomponent Nanopatterns by Directed Block Copolymer Self-Assembly. *ACS Nano* **2013**, *7* (10), 8899–8907.
- (38) Krumrey, M.; Ulm, G. High-Accuracy Detector Calibration at the PTB Four-Crystal Monochromator Beamline. *Nucl. Instrum. Methods Phys. Res. A* **2001**, *467* (468), 1175–1178.
- (39) Wernecke, J.; Krumrey, M.; Hoell, A.; Kline, R. J.; Liu, H. K.; Wu, W. L. Traceable GISAXS Measurements for Pitch Determination of a 25 Nm Self-Assembled Polymer Grating. *J. Appl. Crystallogr.* **2014**, *47* (6), 1912–1920.
- (40) Beckhoff, B. Reference-Free X-Ray Spectrometry Based on Metrology Using Synchrotron Radiation. *J. Anal. At. Spectrom.* **2008**, *23* (6), 845–853.
- (41) Cara, E.; Hönicke, P.; Kayser, Y.; Lindner, J. K. N.; Castellino, M.; Murataj, I.; Porro, S.; Angelini, A.; De Leo, N.; Pirri, C. F.; Beckhoff, B.; Boarino, L.; Ferrarese Lupi, F. Developing Quantitative Nondestructive Characterization of Nanomaterials: A Case Study on Sequential Infiltration Synthesis of Block Copolymers. *ACS Appl. Polym. Mater.* **2023**, *5* (3), 2079–2087.
- (42) Scholze, F.; Procop, M. Modelling the Response Function of Energy Dispersive X-Ray Spectrometers with Silicon Detectors. *X-Ray Spectrometry* **2009**, *38* (4), 312–321.
- (43) Scholze, F.; Procop, M. Detection Efficiency of Energy-Dispersive Detectors with Low-Energy Windows. *X-Ray Spectrometry* **2005**, *34* (6), 473–476.
- (44) Hönicke, P.; Unterumsberger, R.; Wauschkuhn, N.; Krämer, M.; Beckhoff, B.; Indelicato, P.; Sampaio, J.; Marques, J. P.; Guerra,

- M.; Parente, F.; Santos, J. P. Experimental and Theoretical Approaches for Determining the K-Shell Fluorescence Yield of Carbon. *Radiat. Phys. Chem.* **2023**, *202*, No. 110501.
- (45) Nečas, D.; Klapetek, P. Gwyddion: An Open-Source Software for SPM Data Analysis. *Central European Journal of Physics* **2012**, *10* (1), 181–188.
- (46) Müller-Buschbaum, P. GISAXS and GISANS as Metrology Technique for Understanding the 3D Morphology of Block Copolymer Thin Films. *Eur. Polym. J.* **2016**, *81*, 470–493.
- (47) Fernandez-Regu Lez, M.; Solano, E.; Evangelio, L.; Gottlieb, S.; Pinto-Gomez, C.; Rius, G.; Fraxedas, J.; Gutierrez-Fernandez, E.; Nogales, A.; Garcia-Gutierrez, M. C.; Ezquerra, T. A.; Perez-Murano, F. Self-Assembly of Block Copolymers under Nonisothermal Annealing Conditions as Revealed by Grazing-Incidence Small-Angle X-Ray Scattering. *J. Synchrotron Radiat* **2020**, *27*, 1278–1288.
- (48) Ferrarese Lupi, F.; Giammaria, T. J.; Seguíni, G.; Vita, F.; Francescangeli, O.; Sparnacci, K.; Antonioli, D.; Gianotti, V.; Laus, M.; Perego, M. Fine Tuning of Lithographic Masks through Thin Films of PS-b -PMMA with Different Molar Mass by Rapid Thermal Processing. *ACS Appl. Mater. Interfaces* **2014**, *6* (10), 7180–7188.
- (49) Freychet, G.; Maret, M.; Fernandez-Regulez, M.; Tiron, R.; Gharbi, A.; Nicolet, C.; Gergaud, P. Morphology of Poly(Lactide)-Block-Poly(Dimethylsiloxane)-Block-Polylactide High- χ Triblock Copolymer Film Studied by Grazing Incidence Small-Angle X-Ray Scattering. *J. Polym. Sci.* **2020**, *58* (15), 2041–2050.
- (50) Ferrarese Lupi, F.; Giammaria, T. J.; Seguíni, G.; Vita, F.; Francescangeli, O.; Sparnacci, K.; Antonioli, D.; Gianotti, V.; Laus, M.; Perego, M. Fine Tuning of Lithographic Masks through Thin Films of PS-b -PMMA with Different Molar Mass by Rapid Thermal Processing. *ACS Appl. Mater. Interfaces* **2014**, *6* (10), 7180–7188.
- (51) Koo, K.; Ahn, H.; Kim, S. W.; Ryu, D. Y.; Russell, T. P. Directed Self-Assembly of Block Copolymers in the Extreme: Guiding Microdomains from the Small to the Large. *Soft Matter* **2013**, *9* (38), 9059–9071.
- (52) Smilgies, D. M. Scherrer Grain-Size Analysis Adapted to Grazing-Incidence Scattering with Area Detectors. *J. Appl. Crystallogr.* **2009**, *42* (6), 1030–1034.
- (53) Doerk, G. S.; Li, R.; Fukuto, M.; Rodriguez, A.; Yager, K. G. Thickness-Dependent Ordering Kinetics in Cylindrical Block Copolymer/Homopolymer Ternary Blends. *Macromolecules* **2018**, *51* (24), 10259–10270.
- (54) Pospelov, G.; Van Herck, W.; Burle, J.; Carmona Loaiza, J. M.; Durniak, C.; Fisher, J. M.; Ganeva, M.; Yurov, D.; Wuttke, J. BornAgain: Software for Simulating and Fitting Grazing-Incidence Small-Angle Scattering. *J. Appl. Crystallogr.* **2020**, *53*, 262–276.
- (55) Cristofolini, L. Synchrotron X-Ray Techniques for the Investigation of Structures and Dynamics in Interfacial Systems. *Curr. Opin. Colloid Interface Sci.* **2014**, *19* (3), 228–241.
- (56) Beckhoff, B.; Fliegau, R.; Kolbe, M.; Müller, M.; Weser, J.; Ulm, G. Reference-Free Total Reflection X-Ray Fluorescence Analysis of Semiconductor Surfaces with Synchrotron Radiation. *Anal. Chem.* **2007**, *79* (20), 7873–7882.
- (57) Müller, M.; Hönicke, P.; Detlefs, B.; Fleischmann, C. Characterization of High-k Nanolayers by Grazing Incidence X-Ray Spectrometry. *Materials* **2014**, *7* (4), 3147–3159.
- (58) Andrlé, A.; Hönicke, P.; Gwalt, G.; Schneider, P. I.; Kayser, Y.; Siewert, F.; Soltwisch, V. Shape-and Element-Sensitive Reconstruction of Periodic Nanostructures with Grazing Incidence x-Ray Fluorescence Analysis and Machine Learning. *Nanomaterials* **2021**, *11* (7), 1647.
- (59) Peng, Q.; Tseng, Y. C.; Long, Y.; Mane, A. U.; DiDonna, S.; Darling, S. B.; Elam, J. W. Effect of Nanostructured Domains in Self-Assembled Block Copolymer Films on Sequential Infiltration Synthesis. *Langmuir* **2017**, *33* (46), 13214–13223.
- (60) Hönicke, P.; Detlefs, B.; Nolot, E.; Kayser, Y.; Mühle, U.; Pollakowski, B.; Beckhoff, B. Reference-Free Grazing Incidence x-Ray Fluorescence and Reflectometry as a Methodology for Independent Validation of x-Ray Reflectometry on Ultrathin Layer Stacks and a Depth-Dependent Characterization. *Journal of Vacuum Science & Technology A* **2019**, *37* (4), No. 041502.
- (61) Kayser, Y.; Osán, J.; Hönicke, P.; Beckhoff, B. Reliable Compositional Analysis of Airborne Particulate Matter beyond the Quantification Limits of Total Reflection X-Ray Fluorescence. *Anal. Chim. Acta* **2022**, *1192*, 339367.
- (62) Joubert, O.; Fiori, C.; Oberlin, J. C.; Paniez, P.; Pelletier, J.; Pons, M.; Vachette, T.; Weill, A. Resist Degradation under Plasma Exposure: Synergistic Effects of Ion Bombardment. *J. Appl. Phys.* **1991**, *69* (3), 1697–1702.
- (63) Bès, A.; Koo, M.; Phan, T. L.; Lacoste, A.; Pelletier, J. Oxygen Plasma Etching of Hydrocarbon-like Polymers: Part I Modeling. *Plasma Processes and Polymers* **2018**, *15* (8), No. 1800038, DOI: 10.1002/ppap.201800038.
- (64) Müller, M.; Gerlach, M.; Holfelder, I.; Hönicke, P.; Lubeck, J.; Nutsch, A.; Pollakowski, B.; Streeck, C.; Unterumsberger, R.; Weser, J.; Beckhoff, B. X-Ray Spectrometry with Synchrotron Radiation. *PTB - Mitteilungen Forschen und Prüfen* **2014**, *124* (4), 17–23.
- (65) Kucheyev, S. O.; Van Buuren, T.; Baumann, T. F.; Satcher, J. H.; Willey, T. M.; Meulenber, R. W.; Felner, T. E.; Poco, J. F.; Gammon, S. A.; Terminello, L. J. Electronic Structure of Titania Aerogels from Soft X-Ray Absorption Spectroscopy. *Phys. Rev. B Condens Matter Mater. Phys.* **2004**, *69* (24), 1–7.
- (66) Bendavid, A.; Martin, P. J. Review of Thin Film Materials Deposition by the Filtered Cathodic Vacuum Arc Process at CSIRO. *Journal of the Australian Ceramic Society* **2014**, *50* (1), 86–101.
- (67) Niilisk, A.; Moppel, M.; Pärs, M.; Sildos, I.; Jantson, T.; Avarmaa, T.; Jaaniso, R.; Aarik, J. Structural Study of TiO₂ Thin Films by Micro-Raman Spectroscopy. *Central European Journal of Physics* **2006**, *4* (1), 105–116.
- (68) Ottermann, C. R.; Bange, K. Correlation between the Density of TiO₂ Films and Their Properties. *Thin Solid Films* **1996**, *286* (1–2), 32–34.
- (69) Busani, T.; Devine, R. A. B. Dielectric and Infrared Properties of TiO₂ Films Containing Anatase and Rutile. *Semicond. Sci. Technol.* **2005**, *20* (8), 870–875.
- (70) Anderson, O.; Ottermann, C. R.; Kuschnerreit, R.; Hess, P.; Bange, K. Density and Young's Modulus of Thin TiO₂ Films. *Fresenius J. Anal. Chem.* **1997**, *358* (1–2), 315–318.